Hydrogen Spillover between Single Gold Nanorods and Metal Oxide Supports: A Surface Plasmon Spectroscopy Study

Sean S. E. Collins,[†] Michela Cittadini,[‡] Carlos Pecharromán,[§] Alessandro Martucci,[‡] and Paul Mulvaney*[,†]

[†]School of Chemistry & Bio21 Institute, University of Melbourne, Parkville, VIC 3010, Australia, [‡]INSTM and Dipartimento di Ingegneria Industriale, Università di Padova, Via Marzolo 9, 35131 Padova, Italy, and [§]Instituto de Ciencia de Materiales de Madrid (CSIC), C/Sor Juana Inés de la Cruz 3, 28049 Madrid, Spain

ABSTRACT We used dark field spectroscopy to monitor the dissociation of hydrogen on single gold nanoparticles embedded in metal oxide supports. Individual gold nanorods were monitored in real time to reveal the peak position, the full width at half-maximum, and the relative intensity of the surface plasmon resonances during repeated N_2—H_2—N_2 and air—H_2—air cycles. Shifts in the spectra are shown to be due to changes in electron density and not to refractive index shifts in the environment. We demonstrate that hydrogen does not dissociate on gold nanorods (13 nm × 40 nm) at room temperature when in contact with silica and that electrons or hydrogen atoms migrate from Pt nanoparticles to Au nanoparticles through the supporting metal oxide at room temperature. However, this spillover mechanism only occurs for semiconducting oxides (anatase TiO_2 and ZnO) and does not occur for Au and Pt nanoparticles embedded in silica. Finally, we show that hydrogen does dissociate directly on anatase surfaces at room temperature during air—H_2—air cycles. Our results show that hydrogen spillover, surface dissociation of reactants, and surface migration of chemical intermediates can be detected and monitored in real time at the single particle level.

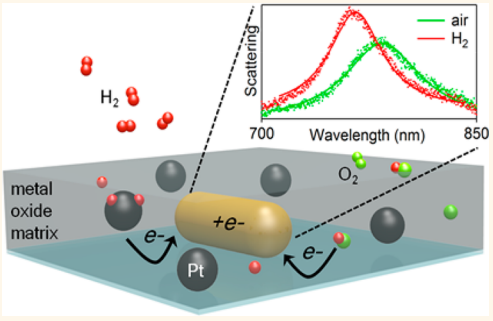

KEYWORDS: hydrogen adsorption · catalysis support effect · gas sensing · surface plasmon spectroscopy · thin films · spillover

Over the past decade, shape-controlled synthesis of nanoparticles (NPs) has opened up the possibility to study heterogeneous catalysis on a variety of well-defined nanoscale crystal facets. The first step in heterogeneous gas catalysis usually involves the adsorption of a reactant onto a catalyst surface. A particularly important case is dissociative H_2 adsorption,[1] which is well documented to occur on transition-metal surfaces, producing mobile adsorbed H atoms.[2] These mobile surface H atoms play a central role in many catalytic processes such as hydrogenation reactions, and understanding their chemical behavior is technologically important for high-density hydrogen storage[3] and for the development of hydrogen-sensing materials.[4] The discovery that mobile H atoms can migrate from the metal to the support matrix and then undergo further chemical reactions depending on the nature of the support and the presence of other sorbed species has been pivotal for catalysis. This cross-material migration process has been coined hydrogen spillover. The goal of this work is to show that single-particle surface plasmon spectroscopy (SPS) is a powerful tool for real-time monitoring of catalytic processes and chemical intermediates during surface redox reactions such as hydrogen spillover.

The first evidence of hydrogen spillover was reported by Khoobiar in 1964 when it was observed that WO_3 underwent a color change when it was reduced by H_2, but only in the presence of a Pt catalyst.[5] Since this discovery, H_2 molecule interactions with metal/oxide surfaces have been studied by a variety of techniques in order to understand spillover: product analysis,[6] electrical conductivity,[7] and infrared,[8] nuclear magnetic resonance,[9] electron paramagnetic resonance,[10] and X-ray absorption spectroscopies.[11] Electrical conductivity measurements

* Address correspondence to mulvaney@unimelb.edu.au.

Received for review May 16, 2015 and accepted July 8, 2015.

Published online July 08, 2015
10.1021/acsnano.5b02970

have been important in confirming that in Pt/TiO_2 materials, H atoms can migrate from the Pt to the reducible TiO_2 surface, remaining mobile in either the atomic (H*) or ionic forms (H^+), with the possibility of both forms coexisting on TiO_2. Roland *et al.* showed that increases in conductivity occur in TiO_2 films that are in contact with, but at a suitable distance from, Pt catalysts exposed to H_2.[12] It was postulated that following chemisorption of hydrogen gas there is an initial dissociation to form surface H atoms, some of which further dissociate into mobile electrons that transfer into the conduction band of the titania support, leaving protons bound to surface lattice oxide ions. However, a half century after its discovery, aspects of both spillover and reverse spillover remain contentious, despite thorough investigation *via* numerous experimental techniques. Recent review articles by Prins[13] and Roland *et al.*[14] discuss the challenges and uncertainties that persist in this area, many of which are due to the extreme difficulty of observing spillover directly.

SPS has emerged a new tool to study the chemisorption of gases on metal nanocrystal surfaces.[15,16] Au NPs exhibit strong extinction coefficients in the visible or NIR due to their ability to support a localized surface plasmon resonance (LSPR). The LSPR of Au NPs is sensitive to both dielectric constant changes in the supporting matrix and to changes in electron density on the metal. Both of these effects can be exploited to glean information about adsorption and desorption events. Initial reports used changes in the absorption spectrum of chemically synthesized Au NP ensembles to demonstrate detection and quantitation of reducing gases such as hydrogen and carbon monoxide.[15,17,18] Optical shifts in Au NPs/metal oxide gas sensors are often considered to be the consequence of electron exchange on the metal at the metal/oxide interface, as well as an effect of dielectric changes in the support.[19,20] It is therefore crucial to understand the separate contributions that modifying the free-electron density on the plasmonic particles and the dielectric function of the supporting medium have on LSPR changes. Buso *et al.* and Della Gaspera *et al.* concluded that LSPR changes from H_2 reduction of Au/TiO_2 and $Au/TiO_2/Pt$ films is induced by the production of free electrons and subsequent charge transfer to the Au NPs.[15,21] This conclusion was supported by the work of Carpenter *et al.*, where it was found that this mechanism was the main driver of LSPR shifts on Au/yttrium-stabilized-zirconia films when exposed to H_2.[22] In contrast to LSPR charge transfer driven shifts, Larsson *et al.* attributed changes in the gold particle spectra to H_2 induced dielectric function changes of nearby Pt NPs separated by a SiO_2 support.[23]

More recent studies showed that gas sorption can be followed even at the single particle level by dark-field microscopy (DFM). DFM was first used to measure the interaction of hydrogen with single metal NPs by Liu *et al.*, who used lithographically fabricated systems of single Pd NPs close to the tip of a Au nanoantenna to monitor dielectric changes of the Pd component during hydrogen exposure.[24] Following this, Tang *et al.* revealed the shape dependence of the hydrogen uptake process studying changes to the dielectric function of a Pd shell on Au cores[25] and Tittl *et al.* used silica shell-isolated Au NPs to investigate the dielectric changes during hydridation of a Pd film.[26] However, the fundamental challenge for catalysis is to investigate the more complex problem of the metal catalyst–support interaction.

By measuring electron transfer at the single particle level, we show in this study that the H_2 adsorption mechanism on Au and Pt NPs strongly depends on the metal oxide support (TiO_2, ZnO, and SiO_2). This highly sensitive technique is enabled by the use of low-scattering, thin films prepared by sol–gel synthesis. While DFM has been used previously to directly measure electron transfer,[27,28] this is the first case where charge transfer processes with gas phase reactants on single metal NPs have been measured directly. SPS measurements on single particles have larger signal-to-noise ratios than ensemble measurements when there is a low level of Au NP loading. A low metal loading removes Au NP–Au NP optical coupling, which simplifies the SPS analysis. Furthermore, it enables proximity effects between Au and Pt NPs to be determined in a straightforward manner because a submonolayer of Au NPs on a flat plane has a more uniform, three-dimensional environment than a multilayer or a mixed layer. We use the single-particle spectroscopic information to unambiguously show that hydrogen is mobile and undergoes spillover from Pt to Au NPs.

RESULTS

I. Gold Nanorods on Glass. We begin by investigating the effects of hydrogen gas on the surface plasmon modes of single Au NRs that have been dispersed onto glass slides. In Figure 1a, the change in LSPR peak position (λ_{max}) of a single Au NR is plotted over a 90 min period for both the Au sample (top) and also for the Au/Pt sample (bottom). During this period, the gas flow was switched from either N_2 (green trace) or air (blue trace) to H_2 and back. For the sample that consisted solely of Au NRs on glass (Au) there was no detectable change to λ_{max} during any of the N_2–H_2 or air–H_2 transitions. Conversely, a 2–3 nm blue-shift was observed on single Au NRs in the Au/Pt sample when the gas was switched from air to H_2, requiring approximately 10 min for λ_{max} to reach a stable value under each new gas flow. The N_2–H_2–N_2 trace follows a similar pattern as the air–H_2–air trace for the Au/Pt sample; however, the recovery rate was noticeably slower under N_2. From these results, we conclude that H_2 does not dissociate on Au NRs. Figure 1b shows typical scattering spectra for a single rod in the Au/Pt

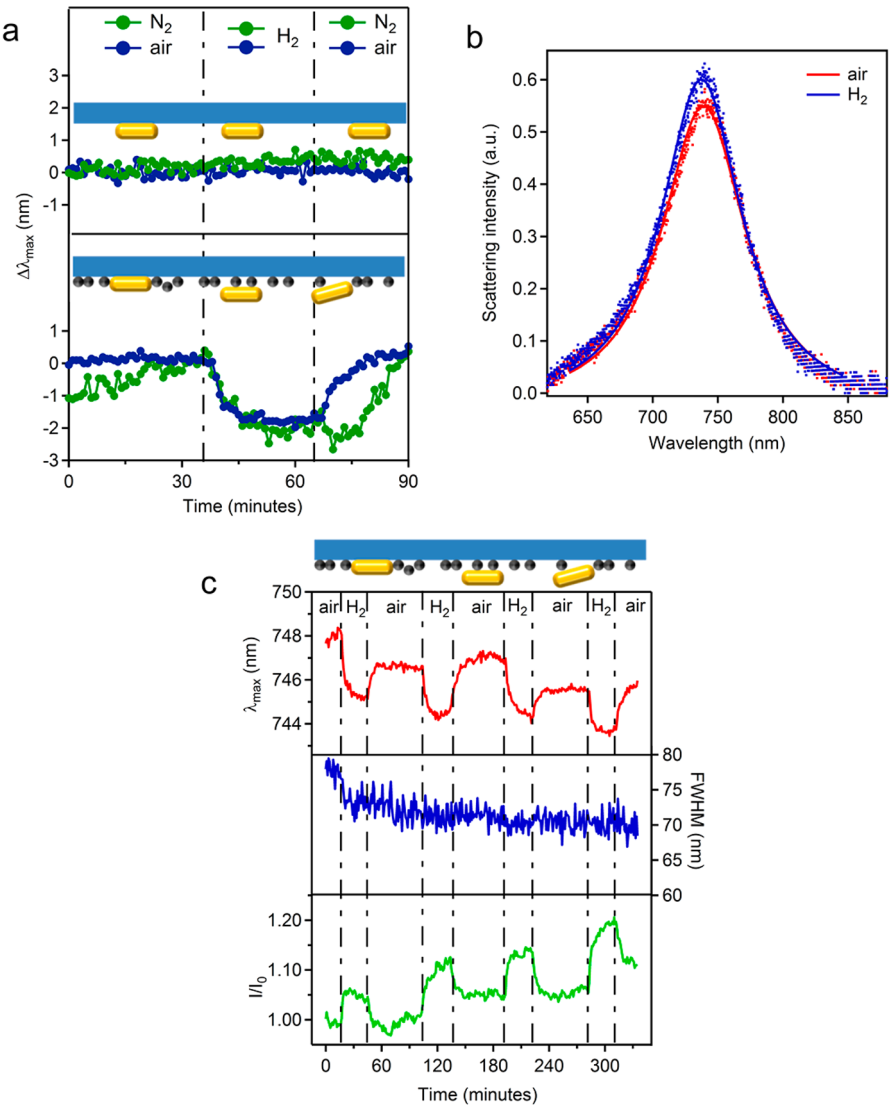

Figure 1. Gas interaction results for a typical single particle on glass in the Au and Au/Pt samples. (a) Comparison of $\Delta\lambda_{max}$ for a single Au NR in the Au sample (top figure) and a single Au NR in the Au/Pt sample in the fourth $N_2-H_2-N_2$ (green) and air$-H_2-$air (blue) cycle. (b) Comparison of scattering spectra for a single Au NR in the Au/Pt sample on the fourth air$-H_2-$air cycle in air (red) and H_2 (blue) after 30 min. (c) Full temporal and spectral analysis of λ_{max} (red), fwhm (blue), and I/I_0 (green) of a single Au NR in the Au/Pt sample during repeated cycles of air$-H_2-$air at rt.

sample after 30 min of exposure, first under air flow (red trace) and then under H_2 flow (blue trace). For the same sample, a 2−3 nm blue-shift was observed upon switching from air to H_2 and this shift was accompanied by an increase of approximately 10% in the peak scattering intensity. Lorentzian fits to the experimental data are also shown. For all samples, peak positions could be calculated to a margin of error of ±0.2 nm.

In Figure 1c, we present traces of λ_{max}, fwhm, and relative peak intensity (I/I_0) as a function of time for a typical single Au NR in the Au/Pt sample over four cycles of air$-H_2-$air flow. After being exposed to air the peak position, λ_{max} blue-shifted repeatedly between 2 and 3 nm during H_2 exposure, consistent with Figure 1a,b. During cycles 1 and 3, λ_{max}, which was partially recovered after H_2 exposure and during cycles 2 and 4, completely recovered to its original position. There was a consistent increase of 5%−10% in the peak-scattered light intensity, I/I_0 (green trace), under H_2 and the scattering intensity reached a stable value at the same rate as λ_{max}. No clear changes occurred in fwhm (blue trace) during any part of the cycle, except following the initial exposure to H_2 which resulted in a small but permanent decrease in fwhm from 77 to 72 nm. It must be noted that changes to λ_{max} only occurred for three out of the five rods measured. Despite the high concentration of Pt NPs deposited onto the glass, it is conceivable that not all Au NRs were in contact with Pt NPs. A full spectral analysis for Au/Pt during four $N_2-H_2-N_2$ cycles is provided in the Supporting Information (Figure S3a).

II. Gold Nanorods in Titania. The presence of a TiO_2 matrix had drastic effects on the spectroscopic behavior of the Au NRs. In Figure 2a, typical scattering spectra for

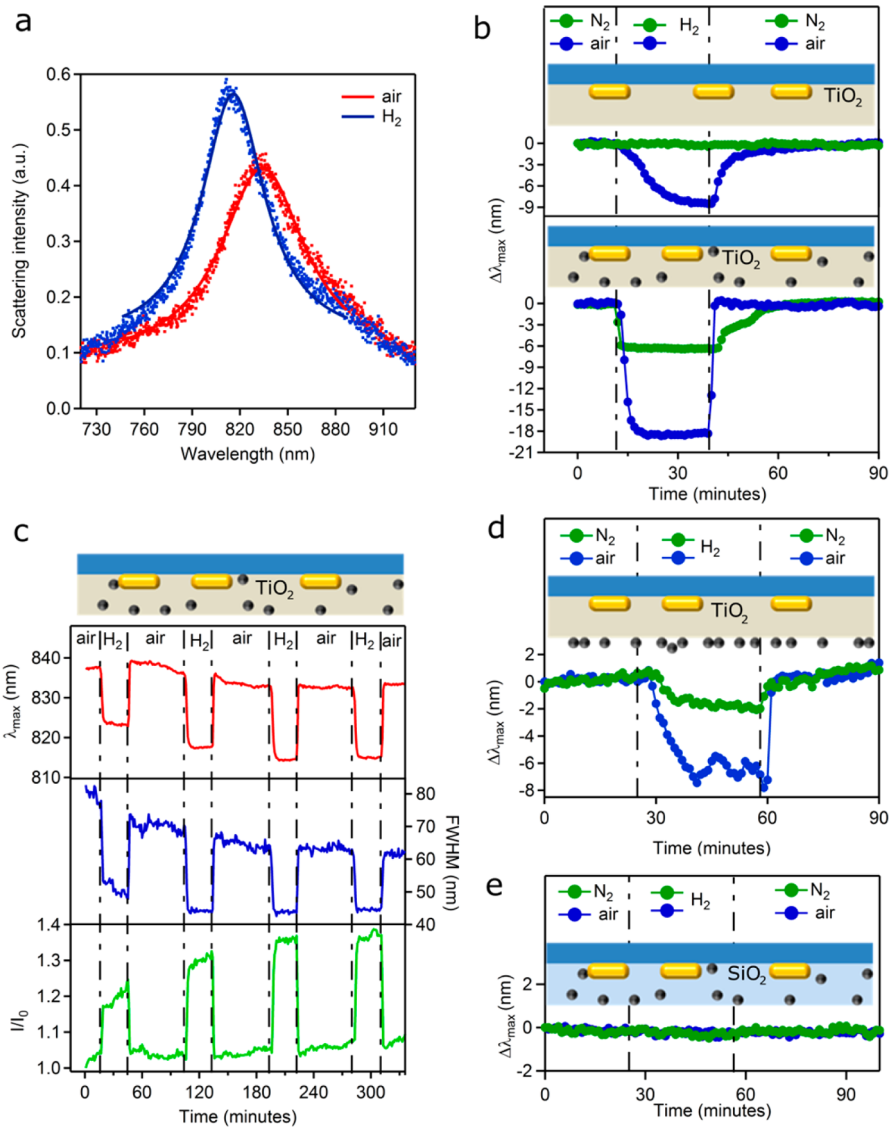

Figure 2. Gas interaction results for a typical single particle in the 30 nm thick Au/TiO_2, 30 nm thick Au/TiO_2−Pt, 30 nm thick Au/TiO_2/Pt, and 100 nm thick Au/SiO_2−Pt samples. (a) Comparison of scattering spectra for a single Au NR in the Au/TiO_2−Pt sample on the fourth air−H_2−air cycle in air (red) and H_2 (blue) after 30 min. (b) Comparison of $\Delta\lambda_{max}$ for a single Au NR in the Au/TiO_2 sample (top) and a single Au NR in the Au/TiO_2−Pt sample (bottom) in the fourth N_2−H_2−N_2 (green) and air−H_2−air (blue) cycle. (c) Full temporal and spectral analysis of λ_{max} (red), fwhm (blue), and I/I_0 (green) of a single Au NR in the Au/TiO_2−Pt sample during repeated cycles of air−H_2−air at rt. Comparison of $\Delta\lambda_{max}$ for a single Au NR in the Au/TiO_2/Pt sample (d) and in the Au/SiO_2−Pt sample (e) in the fourth N_2−H_2−N_2 (green) and air−H_2−air (blue) cycle.

a single rod in the Au/TiO_2−Pt sample are shown after 30 min of exposure first in air flow (red trace) and then under H_2 flow (blue trace). A much larger 19 nm blue-shift was observed upon switching from air to H_2 in the presence of titania, and this was accompanied by an increase of approximately 30% in relative scattering intensity. Figure 2b presents a comparison of $\Delta\lambda_{max}$ for a single Au NR in the Au/TiO_2 sample (top) and a single Au NR in the Au/TiO_2−Pt sample (bottom) during the fourth N_2−H_2−N_2 (green) and air−H_2−air (blue) cycle. Au NRs in the Au/TiO_2−Pt sample exhibited relatively rapid λ_{max} blue-shifts when the gas flow was changed to H_2 from N_2 or air. In the N_2 experiment, the λ_{max} blue-shifted 6 nm over the duration of 2 min in H_2 and the λ_{max} red-shifted upon returning to N_2 although this was markedly slower. During the N_2 phase, the observed peak shifts appeared to undergo a two-step process. In the air experiments, the H_2 induced blue-shifts were stronger than in the N_2 experiments, with an observed shift of 19 nm over a time span of 7 min. The red-shift upon returning to air, in contrast to the N_2 experiment, was faster than the blue-shift and reached a stable value in just 3 min. For the Au/TiO_2 sample that consisted of Au NRs on glass in a TiO_2 matrix there was no detectable change to λ_{max} in the N_2−H_2−N_2. However, during air−H_2−air cycles, the λ_{max} gradually blue-shifted by 9 nm when switched from air to H_2, taking 25 min for λ_{max} to reach a stable value. The red-shift which occurred when the gas flow was returned to air exhibited a similar kinetic trace to the blue-shift.

Figure 2c presents λ_{max}, fwhm, and I/I_0 as a function of time for a typical single Au NR in the Au/TiO_2−Pt sample during four cycles of air−H_2−air flow. The behavior was generally similar to the sample of Au NRs codeposited with Pt NPs on glass; however, the peak shifts and scattering increases were all substantially larger for rods supported on titania. The fwhm (blue trace) followed the same trend kinetic trend as the other two parameters, λ_{max} and I/I_0, but exhibited an average decrease of 20 nm during each exposure of H_2 and subsequently recovered to its original position in air. (For completion, typical results for Au/TiO_2−Pt during four N_2−H_2−N_2 cycles (Figure S3b), as well as Au/TiO_2 during four air−H_2−air cycles (Figure S3c), are provided in the Supporting Information.)

In Figure 2d, we demonstrate the crucial role of the matrix during hydrogen dissociation. There, the Au NRs and Pt NPs were intentionally separated by a 30 nm TiO_2 layer to determine the effect of the relative proximity of the two metal nanoparticles on the spectral response. Au NRs in this sample exhibited a blue-shift of 2 and 7 nm when changing to H_2 from N_2 and air, respectively. We conclude that electron transfer to gold nanoparticles takes place even when dissociation occurs on Pt particles well separated from the gold particle. (A full spectral analysis for experiments on the Au/TiO_2/Pt sample is provided in the Supporting Information, Figures S3d and S3e).

III. Gold Nanorods in Silica and ZnO. In Figure 2e, we present typical scattering data as a function of time for the Au/SiO_2−Pt sample. There was no detectable shift of λ_{max} observed for Au NRs in the Au/SiO_2−Pt sample. We conclude that the silica support does not play an important role in the gas adsorption process.

In addition to TiO_2, we examined ZnO as a supporting matrix to address whether Au NRs in other reducible, semiconducting oxide matrices also exhibit LSPR blue-shifts, increases in scattering and fwhm narrowing under H_2 pressure. There were clear spectral shifts for single Au NRs in the Au/ZnO−Pt sample, demonstrating that ZnO behaves similarly to TiO_2. However, the magnitude of the surface plasmon shifts were not as significant as those observed with the TiO_2-supported samples. A blue-shift of only 3 nm was observed for a typical Au NR in the Au/ZnO−Pt sample when switching from N_2 to H_2 (Figure S3f). This was approximately half of what was observed for the TiO_2 sample. Furthermore, no changes to the spectra of Au NRs in the Au/ZnO sample were observed during air−N_2−air cycles (Figure S3g), which is in contrast to the Au/TiO_2 sample, which blue-shifted upon exposure to H_2 even in the absence of Pt NPs (Figure 2b (top)).

DISCUSSION

The experimental results here demonstrate that spectroscopic changes occur during gas phase redox catalysis which can be used as a method to probe surface reactions. There are two possible explanations for the typical blue-shifts that occur. The first of these is that there is a reduction in the refractive index of the matrix, *e.g.*, conversion of TiO_2 to TiOOH. In this case, the Au NR is acting as a dielectric sensor.[29,30] However, as we show in Figure S4, the refractive index of hydrogen-exposed TiO_2 films is actually slightly higher than that of TiO_2. Consequently, a red-shift would be expected, contrary to what is observed in every experiment on all three different substrates. Furthermore, the increase in refractive index is <0.01, which would not explain the magnitude of the shifts (see Figure S6). A second explanation is that the shift is due to an increase in free electron density on the Au NRs. As shown by calculations presented in Figure S5, increases in electron density on the Au NRs will lead to both a blue-shift and an increase in scattering as observed, and consequently we attribute the spectral shifts in Figures 1 and 2 to changes in electron density.[27,29,31] We cannot exclude the possibility that gas adsorption also leads to small changes in surface scattering of conduction electrons. Adsorbate damping would increase the imaginary component of the Drude term in the dielectric function and this in turn would decrease the intensity of the scattering signal. Desorption of water or surface reactions with organic contaminants may have been the cause of the small 5 nm reduction in fwhm of Au NRs in the Au/Pt sample upon the first exposed to hydrogen. However, this effect alone could not explain the strong blue-shifts and was not observed during subsequent cycles. In the following, we therefore explain the experimental data in terms of electron migration between the catalyst particles.

According to the Drude−Rayleigh equations, a blue-shift in the scattering spectrum is predicted for increased electron density on metal NPs. However, some researchers report that this is accompanied by a decrease in the scattering peak intensity,[32,33] while other groups report an increase.[34] These differences can be reconciled by noting that the changes in scattering intensity depend on the particle aspect ratio. In Figure S5, we present calculated spectra using the Drude−Rayleigh equations for the scattering cross-section of rods with two different aspect ratios. Because the imaginary part of the gold dielectric function is rising with increasing wavelength near 800 nm, we find that a blue-shift leads to less damping and a rise in the peak intensity in accord with our experiments. A slight decrease in fwhm is also predicted, and this decrease is observed in Figure 2c, although the experimental decrease is even larger than predicted and may additional reflect changes in surface scattering. Conversely, for rods with a smaller aspect ratio, the LSPR is located closer to the interband transitions, and here the imaginary part of the dielectric function rises with *decreasing* wavelength. Hence, for these rods, the

blue-shift is accompanied by more damping and a decrease in peak intensity.

SPS provides a rapid diagnostic tool for detecting dissociation of hydrogen on nanocrystal surfaces. The lack of a spectral shift in the control experiment of Figure 1a clearly indicates that H_2 is not able to adsorb dissociatively on Au nanorods supported on glass at room temperature. This is in agreement with literature reports for gold particles of similar dimensions under the experimental conditions used.[35] Dissociation of H_2 on Au has only been observed on NPs below 5 nm.[36,37] When Pt NPs are present, the Au NRs do undergo clear, reversible spectral shifts on glass (Figure 1c). Since the H_2 does not dissociate on the Au NRs, the electrons must be liberated by the Pt particles. However, it is also well established that hydrogen atoms do not migrate on silica. Hence, we deduce that the blue-shift is only possible if the Pt NPs are in contact with, or within a few nanometers of, the Au NRs. Furthermore, the spectrum of the SiO_2 glass supported Au/Pt sample blue-shifted by equal amounts and at similar rates during the H_2 step of the cycle for both O_2 and O_2-free environments, suggesting that H_2 dissociation does not involve oxygen and that the rate of dissociation is unaffected by the presence of oxygen. The reactions producing the surface plasmon shifts on the Au NR may be written as follows:

$$H_2 + (Pt_n)_{SiO_2} \Leftrightarrow 2H\cdots(Pt_n)_{SiO_2} \quad (1)$$

where the molecular hydrogen dissociates on Pt surface to form adsorbed H atoms.

$$2H\cdots(Pt_n)_{SiO_2} + SiO_2 \Leftrightarrow (Pt_n{}^{2-})_{SiO_2} + 2H^+\cdots SiO_2 \quad (2)$$

where H atoms discharge to yield some free electrons with protons bound to surface silica.

$$(Pt_n{}^{2-})_{SiO_2} + (Au_n)_{SiO_2} \Leftrightarrow (Pt_n)_{SiO_2} + (Au_n{}^{2-})_{SiO_2} \quad (3)$$

where electrons migrate between *touching* Au and Pt NPs to equilibrate the Fermi levels.

Note that because free protons cannot form on the Pt surface, it is likely that atomic hydrogen migrates from the Pt surface and is initially adsorbed to anionic sites on the metal oxide support immediately adjacent to the Pt NP (reaction 2). Given that spillover from Pt to defect-free SiO_2 is energetically impossible,[13] the anionic site where H^+ ionosorption occurs is likely to be a lattice O^{2-} ion which is bonded to a Si^{3+} associated with a surface oxygen vacancy ($V_{O^{2-}}{}^{+}$).[38] The proton–electron pairs produced are not mobile on the insulating SiO_2 support. Delocalized electrons are consequently injected only into those Au NRs, which are in direct electrical contact with the Pt. This causes a blue-shift and the increase of the intensity in the plasmon resonance peak of Au NRs in the Au/Pt sample.

The proposed mechanism also explains the results for the Au/SiO_2–Pt sample. In this sample, the Pt NPs are dispersed in a three-dimensional matrix so the chance of one being in contact with a Au NR is strongly diminished. Therefore, although protons and electrons may be produced at $V_{O^{2-}}{}^{+}$ sites, they are not able to be transported to the Au NR, and thus, no change to the spectrum is observed. This result further corroborates the conclusion that dielectric changes to nearby Pt NPs upon Pt–H formation does not contribute significantly to the scattering signals of the rods since shifts should have been observed in the Au/SiO_2–Pt sample, which also had a high concentration of Pt NPs.

Hydrogen Spillover. The results discussed so far have involved Au NRs and Pt NPs in contact with a non-reducible metal oxide support, and these oxides are unable to support hydrogen spillover because the energy required to break a M–H bond is large.[13] Consequently, spillover of atomic H (radical H*) onto the defect-free glass surface does not occur.[39,40] Conversely, TiO_2 is known to be active in the hydrogen spillover process.[41] The results obtained with Au/TiO_2–Pt clearly show an enhancement of the gas interaction compared to all other samples. For the Au/TiO_2–Pt sample we propose that when the measurements were performed in the absence of O_2, reactions 1–3 (with TiO_2 instead of SiO_2) constitute the mechanism of electron transfer. However, dissociation of hydrogen into free conduction electrons additionally enables the transfer of electrons to the gold particles through the semiconducting matrix.

The results from the Au/TiO_2/Pt sample verify that electrons can travel through the semiconductor matrix itself. In this case, the Pt NPs were spatially separated from the Au NRs by a titania film about 30 nm in thickness. A blue-shift was still recorded for all Au NRs examined in H_2 after being in N_2 (Figure 2d, bottom trace). Therefore, since H_2 dissociation was only occurring on the Pt NPs, electrons must be traveling through the TiO_2 to reach the Au NR. The magnitude of the shift when the Pt NPs were separated was approximately three times smaller than for the mixed Pt and TiO_2 sample. This suggests there is a limited range over which interparticle electron transfer occurs and it is probably space charge limited; *i.e.*, as electrons accumulate on gold particles, there is a space charge build-up, which slows down further electron transfer. The flux is limited at this point by the surface migration/diffusion of protons from Pt to the Au.

From our results, we are unable to directly confirm whether or not mobile protons are reacting with the Au NR surfaces and forming Au–H complexes. The dissociation of H_2 and subsequent diffusion onto Au would contribute to the blue-shift observed by also increasing electron density on the Au NRs.[42] Au–H formation has been proposed on particles with diameters larger than 5 nm based on SPS measurements made on gold nanoparticle films. However, these possible measurements of Au–H formation on large Au nanocrystals were observed at high temperatures[43]

or when the energy used to illuminate the gold nanoparticles was sufficiently high enough that hot-electron generation could drive direct H_2 dissociation on the Au surface.[44] Our measurements have been made at room temperature and have been shown not to be influenced by hot-electron processes. Nevertheless, it is still possible that the energy barrier has been lowered enough for Au−H formation to occur when mobile protons on TiO_2 come into contact with edge or corner sites of large Au NRs which could be contributing to the blue-shifts. Further SPS studies into distinguishing between electron and proton interactions with gold nanoparticles would be required to confirm the proposed mechanism.

Anomalous Role of Oxygen. Large blue-shifts of the LSPR peak occurred under H_2 flow for Au/TiO_2, in the absence of Pt NPs, but only when the sample was exposed to air flow beforehand. When oxygen was removed from the reaction the spectra underwent no change during gas cycling (Figure 2b, top). Since H_2 does not dissociate on these gold nanoparticles, which do not have a significant fraction of low-coordination-number surface gold atoms,[45,46] this experiment demonstrates that H_2 dissociates on TiO_2 surfaces that have been exposed to oxygen. We propose that reactive oxygen ions generate sites that can enable H_2 to dissociate. It has been previously observed that oxygen can adsorb to the Ti^{3+} on the surface when there are oxygen vacancies $V_{O^{2-}}{}^{+}$ on the surface.[47,48] Changes in the electrical resistance of TiO_2 have also been measured at ~300 K when switching between O_2 and H_2.[50,51] Work carried out by Roland *et al.* clearly shows that there is no change in resistance of TiO_2 when switching to O_2 and H_2 pressures from vacuum,[12] while Li *et al.* have previously reported the enhancement of hydrogen spillover by surface labile oxygen species on Pt/TiO_2 catalysts[49] although the reason is not well understood.[41] Likewise, we find here that the presence of chemisorbed oxygen is required in order for H_2 to generate an LSPR response on anatase. The conductivity and optical changes can be understood in terms of the following mechanism:

$$\frac{1}{2}O_{2(g)} + V_{O^{2-}}{}^{+} + 3e^{-} \leftrightarrow O^{2-}{}_{(ads)} \quad (4)$$

where oxygen molecules adsorb onto $V_{O^{2-}}{}^{+}$ sites on the TiO_2 surface to generate chemisorbed oxygen ions.

$$H_2 + 2O^{2-}{}_{(ads)} \leftrightarrow 2OH^{-}{}_{(ads)} + 2e^{-} \quad (5)$$

where H_2 slowly dissociates on the TiO_2 surfaces where reactive oxygen ions are adsorbed.

Reaction 5 creates hydroxyl groups on the surface of the titania and generates free conduction electrons.

Hydrogen Spillover on ZnO. The Au/ZnO and Au/ZnO−Pt samples behaved similarly to the equivalent TiO_2 samples; however, ZnO was not as effective as TiO_2 at facilitating spillover. Fewer electrons were injected into the Au NRs when surrounded by a ZnO matrix. Without any Pt NPs present, even in an O_2-rich environment, Au NRs in a ZnO matrix did not undergo any LSPR changes. The results from the air−H_2−air cycles suggest that the ZnO cannot lower the reaction pathway enough to allow reaction 4 to occur at a measurable level. This may be attributed to the fact that, because of its unfilled d orbital, the Ti^{3+} sites are more acidic than the Zn^{+} sites.

CONCLUSIONS

Further progress toward rational catalysis design will depend on the emergence of new methods for understanding and measuring chemical reactions on the surface of nanoscale heterogeneous catalysts such as noble metal NPs. This work has capitalized on the flexibility of DFM to measure electron transport and catalysis mechanisms in colloidal thin films at the single particle level. Isolating heterogeneous catalysis measurements to a single particle in various matrices has the ability to direct design for new supported catalyst systems. We have demonstrated here that we can monitor gas dissociation and charge migration between single nanocrystal particles during hydrogen adsorption. Furthermore, we see direct evidence for the crucial role of the metal oxide support matrix. Au NRs only function as an optical electron-transfer probe in our experiments as they played no active role in the H_2 gas adsorption. We have demonstrated that it is possible for electrons to be transported from Pt NPs during hydrogen dissociation to single Au NRs *via* a semiconducting matrix. The matrix also greatly enhances the number of electrons transferred and also accelerates the kinetics of forward and back electron transfer. The presence of adsorbed oxygen species can also lead to the generation of free conduction electrons in the presence of hydrogen gas, which provides a second mechanism for electron transfer to the gold nanocrystals.

EXPERIMENTAL SECTION

Synthesis of TiO_2 NPs. TiO_2 NPs with 10 nm diameters were synthesized as previously described[50] by adding 3.08 g of titanium tetraisopropoxide ($Ti(OPr)_4$, Aldrich, 97%) into a previously prepared solution containing 1.24 g of water (Milli-Q, 18.2 MΩ/cm), 1.78 g of hydrochloric acid aqueous solution (HCl, Ajax Chemicals, 36%), and 7.18 g of methanol (Merck, AR grade). The solution was stirred for 60 min at room temperature (rt) and heated in an oil bath at 70 °C for 4 h under reflux. The suspension was cooled to room temperature, and the particles were precipitated by adding 30.6 g of acetone (Unilab, AR grade). The precipitate was collected by centrifuging the solution at 4000 rpm for 2 min. After the supernatant was discarded,

the wet precipitate was dispersed in 26 mL of methanol, yielding a clear 8 mg/mL TiO_2 anatase sol.

Preparation of SiO_2 Sol–Gel. A silica sol was prepared by mixing 5.78 g of tetraethyl orthosilicate ($(Si(OC_2H_5)_4$, TEOS, Aldrich, 98%), 2.58 g of ethanol (Merck, AR grade), 2 g of water, and 32 mg of 36% hydrochloric acid aqueous solution. The mixed solution was allowed to stir at room temperature for 1 h before deposition.

Synthesis of ZnO NPs. ZnO NPs with 10 nm diameter were synthesized as previously described[51] by dissolving 500 mg of zinc acetate dihydrate (Aldrich, ≥98%) in 22.5 mL of dimethyl sulfoxide (Chem Supply, AR grade). Separately, 750 mg of tetramethylammonium hydroxide (TMAH, Aldrich, 97%) was dissolved in 7.5 mL of ethanol. The TMAH solution was added dropwise (2 mL/min) to the zinc solution under vigorous stirring at room temperature. After 10 min, the solution was heated at 50 °C for 1 h. Then the solutions were cooled to room temperature, precipitated with 90 mL of methyl ethyl ketone (Ajax Chemicals, AR grade), and centrifuged at 1500 rpm for 5 min. The supernatant was removed, and the precipitate was redispersed in 2.84 mL of ethanol to a final concentration of 0.8 M in zinc ions.

Synthesis of Gold Nanorods. Gold nanorods (Au NRs), with diameters of 13 ± 4 nm and lengths of 40 ± 9 nm (see Figure S1) were prepared according to the seed-mediated method proposed by Nikoobakht *et al.*[52] The seed solution was prepared by initially mixing 5 mL of a 0.2 M cetyltrimethylammonium bromide (CTAB, Unilab, 98%) aqueous solution with 5 mL of a 0.5 mM aqueous solution of gold(III) chloride ($HAuCl_4.3H_2O$, Aldrich, ≥ 99.9%). Under stirring of the mixed solution, 0.6 mL of ice-cold 0.01 M $NaBH_4$ (Aldrich, 98.5%) was added and the solution vigorously stirred for a further 2 min. The seed solution was stored at rt and used within 4 h of preparation. A growth solution was prepared by adding 5 mL of 0.2 M CTAB to 0.2 mL of 4 mM $AgNO_3$ (Sigma-Aldrich, ≥ 99.0%) at rt. To this growth solution was added 5 mL of 1 mM $HAuCl_4$, and after mixing of the solution, 70 μL of 79 mM L-ascorbic acid (BDH Chemicals, 98.7%) was added and the solution vigorously mixed for 5 s. Immediately, 12 μL of the seed solution was added to the growth solution and the solution vigorously mixed for 5 s. The growth solution was then left in a water bath at 30 °C for 16 h. The solution was then centrifuged twice at 8000 rpm for 20 min, and 9 mL (~90%) of the supernatant was removed. Nine milliliters of water was added back to the precipitate and redispersed sequentially. The final solution was diluted 10 times from the as-synthesized concentration. The estimated nanoparticle concentration of the Au NR solution used for spin coating was 2.5×10^{-11} M based on yields reported by Orendorff *et al.*[53]

Synthesis of Pt NPs. Platinum colloids of 10 nm diameter were prepared using the polyol method.[54,55] A 1 mL solution of 80 mM chloroplatinic acid hydrate (H_2PtCl_6, Aldrich, 99.9%) was rapidly added to 7 mL of ethylene glycol (Sigma-Aldrich, anhydrous, 99.8%) with 30 mM and 90 mM concentrations of poly(vinylpyrrolidone) (PVP, Aldrich, MW = 10000) and $NaNO_3$ (Unilab, 97%), respectively, at 160 °C. After 30 min, the NP solution was cooled to rt and precipitated with excess acetone (Unilab, AR grade). The solution was centrifuged at 4000 rpm for 5 min, the supernatant discarded, and the precipitate redispersed in ethanol to produce a 30 mM sol based on the Pt ion content.

Preparation of Films. Samples were deposited on 1 mm thick fused silica quartz glass slides for DFM measurements and on silicon substrates for ellipsometry and SEM measurements. A summary of the various samples for DFM is provided in Table 1. The Au sample was prepared by spin coating the aqueous Au NR solution at 3000 rpm for 30 s and then drying the sample at 70 °C for 10 min. The Au/Pt sample was prepared by spin coating the Pt NPs containing ethanol solution at 3000 rpm for 30 s and annealing the sample at 150 °C for 10 min. Following this, the aqueous solution of Au NRs was spin coated on to the Pt NPs monolayer, in the same manner as the Au sample, and annealed at 70 °C. The Pt NPs, requiring a high annealing temperature to work effectively as a catalyst, were deposited first, while the Au NRs are known to spheroidize at temperatures higher than 80 °C; this restriction determined the order of the layers. This restriction was overcome by covering the Au NRs with the TiO_2 matrix, enabling an increase in the annealing temperature up to 150 °C, avoiding the Au NR spheroidization.

TABLE 1. Order of the Layers and the Material Composition for the Eight Different Samples Prepared for Optical Measurements[a]

Sample	Sample name	Composition	Schematic
A	Au	Bare AuNRs on glass	
B	Au/Pt	Au NRs and Pt NPs on glass	
C	Au/TiO_2	AuNRs on glass covered with a TiO_2 film	
D	Au/TiO_2-Pt	Au NRs on glass covered with a TiO_2 film containing 8 wt% Pt NPs	
E	Au/ TiO_2/Pt	Au NRs on glass covered with a TiO_2 film with Pt NPs deposited on top	
F	Au/ SiO_2-Pt	Au NRs on glass covered with a SiO_2 film containing 8 wt% Pt NPs	
G	Au/ZnO	Au NRs on glass covered with a ZnO film	
H	Au/ZnO-Pt	Au NRs on glass covered with a ZnO film containing 8 wt% Pt NPs	

[a] Dark blue represents the glass substrate in the schematic, gold represents Au NRs, black represents Pt NPs, gray represents TiO_2, light blue represents SiO_2, and light green represents ZnO.

The Au/TiO_2 sample was prepared initially by the same method as the Au sample, with a further layer of TiO_2 NPs deposited at 3000 rpm for 30 s and then annealed at 150 °C for 10 min. The Au/TiO_2–Pt sample was prepared in the same way as the previous sample, except with an ethanolic mixture of TiO_2 and 8 wt % Pt NPs instead of just TiO_2. The Au/TiO_2/Pt sample was prepared by the same method as the Au/TiO_2 sample, except before the annealing step, a submonolayer of Pt NPs (the same volume used to make Au/TiO_2–Pt) was spin coated on the top of the sample. The Au/SiO_2–Pt sample was prepared by spin coating the Au NRs solution as for the bare Au NRs, then, the SiO_2 solution was mixed with the 8 wt % Pt NPs solution, and spin coated on the top of the Au NRs submonolayer and annealed at 150 °C for 10 min. The Au/ZnO and Au/ZnO–Pt samples were prepared by the same method as their TiO_2 counterparts. In all metal oxide films prepared the Au NR concentration is estimated to be <0.25 wt % based on the average interparticle distance observed on the DFM. All thermal annealing was carried out in air.

Characterization. Ensemble absorbance spectra were collected with an Agilent 8453 UV–vis spectrophotometer between 200 and 1000 nm. Optical constants *n* and *k* and film thicknesses were evaluated by measuring the variables Ψ and Δ with a J. A. Wollam V-VASE spectroscopic ellipsometer at two angles of incidence (60° and 70°) in the wavelength range of 300–1500 nm. Optical constants *n* and *k* and film thicknesses were evaluated from Ψ, Δ data using the WVASE32 ellipsometry data analysis software. The data were fitted with Cauchy dispersion and Tauc–Lorentz oscillators in the nonabsorbing region and at the UV absorption edge, respectively. Transmission electron microscopy (TEM) images were acquired on a FEI Tecnai TF20 microscope operating at 200 kV. TEM samples were prepared by drop casting the sample solutions onto copper TEM grids (300 carbon mesh) and drying in ambient conditions. Scanning electron microscopy (SEM) was performed on a FEI Nova 200 Nanolab microscope operating at 5 kV.

Characterization of the Au NRs is reported in Figure S1, from which it is possible to note that the Au NRs had an aspect ratio of 3 with a longitudinal LSPR centered at 810 nm. The refractive indices of the layers used for covering the Au NRs were 1.43, 1.95, and 1.72 for SiO_2, TiO_2, and ZnO, respectively (at 630 nm).

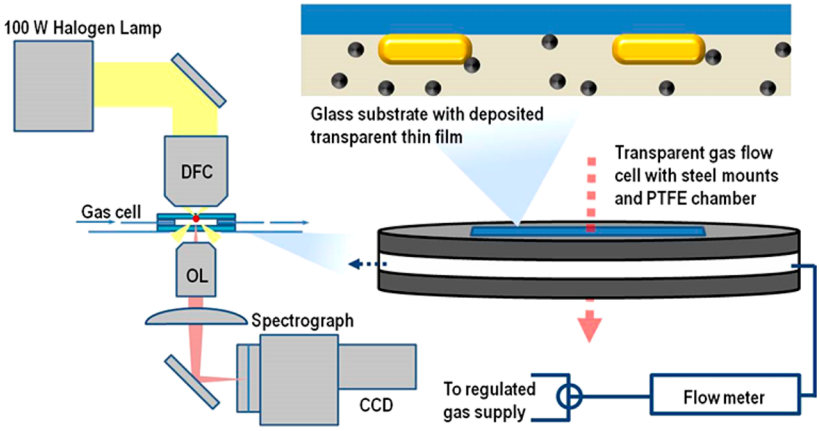

Figure 3. Optical setup for single particle gas measurements. An optical inverted microscope fitted with a dry dark-field condenser (DFC) and 40× objective lens (OL) is coupled to an imaging spectrometer with an array detector (CCD). (Right) Larger view of the home-built transmission gas cell with a microschematic view of a sample thin film on the underside of the top window.

The metal oxide layer thicknesses were 100, 30, and 30 nm for the SiO_2, TiO_2, and ZnO films, respectively. From the SEM images in Figure S2, it is evident that the films were homogeneous and smooth.

Single Particle Spectroscopy Measurements. Single-particle time-resolved measurements were carried out using a Nikon TE2000-S Eclipse inverted microscope equipped with a Nikon dry dark-field condenser and a 40*X*/0.6 NA ELWD dry objective lens in transmission configuration. A Princeton Instruments Isoplane SCT 320 imaging spectrograph fitted with a PIXIS 1024F CCD detector was coupled to the image output of the microscope for spectroscopic measurements (Figure 3). The samples were placed in a custom-made cell in which the scattering spectra could be collected in transmission under different atmospheres. The measurements were taken at room temperature (RT) using 50000 ppm of H_2, balanced with N_2 (5% H_2 in N_2), with a flow rate of 5 L/h. The gases used in these experiments were all high purity grade (<10 vpm C_nH_m) with very low water content (<15 vpm). All $N_2-H_2-N_2$ and air$-H_2-$air cycles were 60 min$-$30 min$-$60 min in duration.

Using the DFM, Au NR spectra were captured every 60 s during four cycles of exposure to 5% H_2 in N_2, with N_2 or air as the alternating gas. The imaging spectroscopy system had the ability to measure the scattering spectra of multiple, well-distributed AuNRs simultaneously enabling the surface plasmon band position of 3$-$10 particles to be tracked at the same time. This provided greater statistical certainty about the spectral response of a typical single particle during each experiment within the same sample, and a typical single particle kinetic trace could therefore be selected to be representative of the sample as a whole. An automated image-to-spectrum extraction and Lorentzian fitting procedure was carried out on the data using IGOR Pro software to execute fast and accurate analysis of hundreds of image files collected during each experiment. Prior to running the procedure, the pixel rows of a Au NR-free area of the image in close proximity to the Au NRs being analyzed was subtracted from the signal to remove the background contribution from the substrate and oxide layer. Examples of the scattering intensity of the background varying with time have been included in the Supporting Information (Figure S7) to illustrate the stability of these signals during the gas cycles. The baseline of the single particle spectra of an oxide supported Au NR did not always reach zero. This is due to the slight inhomogeneity of background scattering that was caused by the oxide matrix and the Pt NPs, and could lead to a less effective background correction. If the background signal that was selected for the procedure had a different level of scattering intensity than the small area the Au NR is situated in, the background correction might not have been completely effective in removing the scattering contribution of the surrounding matrix from the Au NR signal. Nevertheless, regular, quasi-Lorentzian lineshapes at intensities expected for single Au NRs of these dimensions were measurable and Lorentzian fitting could be effectively applied to the data extracted. Hence, while automation resulted in enormous efficiency gains, there was a small but noteworthy drawback in accuracy.

The experiments typically ran for 6 h, which resulted in slow long-term drifts in the focal position of the microscope. Over this time the focal position could influence the absolute value of LSPR peak position due to chromatic aberrations present in the objective lenses. An additional focal drift correction was made by fitting a trend line to the data and normalizing the data to the fit function, where the long-term changes in the data were clearly not due to the introduction of different atmospheres into the gas chamber.

Conflict of Interest: The authors declare no competing financial interest.

APPENDIX.

Scattering Signal. In dark field microscopy, we measure the scattering from single particles, rather than the ensemble extinction spectrum. To determine the scattering, it is easiest to consider the cross-section of a single particle. Within the Rayleigh regime, valid for NPs, the intensity of scattered light, $I_{sca}(\theta)$ at an angle θ is given by

$$I_{sca}(\theta) = I_0 \frac{k^4}{32\pi^2\varepsilon_m^2 r^2}|\alpha|^2(1+\cos^2\theta) \qquad \text{(A1)}$$

where $k = 2\pi/\lambda$, I_0 is the incident light intensity, r is the distance to the detector, ε_m is the dielectric constant of the non-absorbing medium, and the polarizability of the nanocrystal is given by

$$\alpha = 3\varepsilon_m \frac{\varepsilon_p - \varepsilon_m}{\varepsilon_p + \frac{(1-L)}{L}\varepsilon_m} V \qquad \text{(A2)}$$

Here, V is the particle volume and ε_p is the complex dielectric function of the particle, which can be approximated by the Drude model, which works well for gold and is linearly proportional to the electron density, especially at VIS and IR frequencies. In this regard, eq A1 exhibits a peak at almost exactly the same wavelength or frequency as the absorption spectrum

of an ensemble of the particles. Increasing the electron density N (and consequently ε_p) leads to a blue-shift in the scattered peak, an increase in the intensity of the scattering signal, and a decrease in the FWHM of the scattered light spectra, as shown in Figure S5. This is true only for particles characterized by $L < 0.08$, with resonances at wavelengths longer than 600 nm in water. For $L > 0.08$, the SPR resonance is situated close to the interband transitions and for these particles, an increase in N leads to a blue-shift as expected, but due to the increased damping of the conduction oscillations, the scattering peak decreases in intensity and there is a slight broadening of the spectra.

Supporting Information Available: Optical and structural characterization of Au nanorods, film characterization, additional spectroscopy results, and ellipsometry results. The Supporting Information is available free of charge on the ACS Publications website at DOI: 10.1021/acsnano.5b02970.

Acknowledgment. P.M. thanks the ARC for support through Grant No. LF100100117. We are grateful to the USAF AOARD for support through Grant No. FA2386-13-1-4072. We thank Harald Giessen for useful discussions.

REFERENCES AND NOTES

1. Christmann, K. Interaction of Hydrogen with Solid-Surfaces. *Surf. Sci. Rep.* **1988**, *9*, 1–163.
2. Nordlander, P.; Holloway, S.; Norskov, J. K. Hydrogen Adsorption on Metal-Surfaces. *Surf. Sci.* **1984**, *136*, 59–81.
3. Wang, L.; Yang, R. T. New Sorbents for Hydrogen Storage by Hydrogen Spillover – A Review. *Energy Environ. Sci.* **2008**, *1*, 268–279.
4. Morrison, S. R. Semiconductor Gas Sensors. *Sens. Actuators* **1981**, *2*, 329–341.
5. Khoobiar, S. Particle to Particle Migration of Hydrogen Atoms on Platinum—Alumina Catalysts from Particle to Neighboring Particles. *J. Phys. Chem.* **1964**, *68*, 411–412.
6. Beck, D. D.; White, J. M. Spillover of Deuterium on Platinum/Titanium Dioxide. 1. Dependence on Temperature, Pressure, and Exposure. *J. Phys. Chem.* **1984**, *88*, 2764–2771.
7. Herrmann, J. M.; Pichat, P. Evidence by Electrical Conductivity Measurements for Hydrogen Spill Over on Pt, Rh and Ni/TiO_2 Catalysts. Consequences for Bifunctional Photocatalysis. *Stud. Surf. Sci. Catal.* **1983**, *17*, 77–87.
8. Cavanagh, R.; Yates, J. T., Jr. Hydrogen Spillover on Alumina - A Study by Infrared Spectroscopy. *J. Catal.* **1981**, *68*, 22–26.
9. Lenz, D.; Conner, W. C., Jr.; Fraissard, J. P. Hydrogen Spillover on Silica III. Detection of Spillover by Proton NMR. *J. Catal.* **1989**, *117*, 281–289.
10. Sermon, P. A.; Bond, G. C. Studies of Hydrogen Spillover. Part 1.—Study of the Rate, Extent and Products of Hydrogen Spillover from Platinum to the Trioxides of Tungsten and Molybdenum. *J. Chem. Soc., Faraday Trans. 1* **1976**, *72*, 730–744.
11. Bus, E.; Miller, J. T.; van Bokhoven, J. A. Hydrogen Chemisorption on Al_2O_3-Supported Gold Catalysts. *J. Phys. Chem. B* **2005**, *109*, 14581–14587.
12. Roland, U.; Salzer, R.; Braunschweig, T.; Roessner, F.; Winkler, H. Investigations on Hydrogen Spillover. Part 1: Electrical Conductivity Studies on Titanium Dioxide. *J. Chem. Soc., Faraday Trans.* **1995**, *91*, 1091–1095.
13. Prins, R. Hydrogen Spillover. Facts and Fiction. *Chem. Rev.* **2012**, *112*, 2714–2738.
14. Roland, U.; Braunschweig, T.; Roessner, F. On the Nature of Spilt-Over Hydrogen. *J. Mol. Catal. A: Chem.* **1997**, *127*, 61–84.
15. Della Gaspera, E.; Bersani, M.; Mattei, G.; Nguyen, T. L.; Mulvaney, P.; Martucci, A. Cooperative Effect of Au and Pt Inside TiO_2 Matrix for Optical Hydrogen Detection at Room Temperature Using Surface Plasmon Spectroscopy. *Nanoscale* **2012**, *4*, 5972–5979.
16. Langhammer, C.; Larsson, E. M.; Kasemo, B.; Zoric, I. *Nanoplasmonic Sensors*; Springer: New York, 2012; pp 169–197.
17. Ando, M.; Kobayashi, T.; Haruta, M. Enhancement in the Optical CO Sensitivity of NiO Film by the Deposition of Ultrafine Gold Particles. *J. Chem. Soc., Faraday Trans.* **1994**, *90*, 1011–1013.
18. Ando, M.; Kobayashi, T.; Iijima, S.; Haruta, M. Optical Recognition of CO and H_2 by Use of Gas-Sensitive Au–Co_3O_4 Composite Films. *J. Mater. Chem.* **1997**, *7*, 1779–1783.
19. Dharmalingam, G.; Joy, N. A.; Grisafe, B.; Carpenter, M. A. Plasmonics-Based Detection of H_2 and CO: Discrimination Between Reducing Gases Facilitated by Material Control. *Beilstein J. Nanotechnol.* **2012**, *3*, 712–721.
20. Joy, N. A.; Nandasiri, M. I.; Rogers, P. H.; Jiang, W.; Varga, T.; Kuchibhatla, S. V.; Thevuthasan, S.; Carpenter, M. A. Selective Plasmonic Gas Sensing: H_2, NO_2, and CO Spectral Discrimination by a Single Au-CeO_2 Nanocomposite Film. *Anal. Chem.* **2012**, *84*, 5025–5034.
21. Buso, D.; Post, M.; Cantalini, C.; Mulvaney, P.; Martucci, A. Gold Nanoparticle-Doped TiO_2 Semiconductor Thin Films: Gas Sensing Properties. *Adv. Funct. Mater.* **2008**, *18*, 3843–3849.
22. Baltrus, J. P.; Ohodnicki, P. R.; Joy, N. A.; Carpenter, M. A. Examination of Charge Transfer in Au/YSZ for High-Temperature Optical Gas Sensing. *Appl. Surf. Sci.* **2014**, *313*, 19–25.
23. Larsson, E. M.; Langhammer, C.; Zoric, I.; Kasemo, B. Nanoplasmonic Probes of Catalytic Reactions. *Science* **2009**, *326*, 1091–1094.
24. Liu, N.; Tang, M. L.; Hentschel, M.; Giessen, H.; Alivisatos, A. P. Nanoantenna-Enhanced Gas Sensing in a Single Tailored Nanofocus. *Nat. Mater.* **2011**, *10*, 631–636.
25. Tang, M. L.; Liu, N.; Dionne, J. A.; Alivisatos, A. P. Observations of Shape-Dependent Hydrogen Uptake Trajectories from Single Nanocrystals. *J. Am. Chem. Soc.* **2011**, *133*, 13220–13223.
26. Tittl, A.; Yin, X.; Giessen, H.; Tian, X. D.; Tian, Z. Q.; Kremers, C.; Chigrin, D. N.; Liu, N. Plasmonic Smart Dust for Probing Local Chemical Reactions. *Nano Lett.* **2013**, *13*, 1816–1821.
27. Novo, C.; Funston, A. M.; Mulvaney, P. Direct Observation of Chemical Reactions on Single Gold Nanocrystals Using Surface Plasmon Spectroscopy. *Nat. Nanotechnol.* **2008**, *3*, 598–602.
28. Eo, M.; Baek, J.; Song, H. D.; Lee, S.; Yi, J. Quantification of Electron Transfer Rates of Different Facets on Single Gold Nanoparticles during Catalytic Reactions. *Chem. Commun.* **2013**, *49*, 5204–6.
29. Mulvaney, P. Surface Plasmon Spectroscopy of Nanosized Metal Particles. *Langmuir* **1996**, *12*, 788–800.
30. Lee, K. S.; El-Sayed, M. A. Gold and Silver Nanoparticles in Sensing and Imaging: Sensitivity of Plasmon Response to Size, Shape, and Metal Composition. *J. Phys. Chem. B* **2006**, *110*, 19220–19225.
31. Rogers, P. H.; Sirinakis, G.; Carpenter, M. A. Direct Observations of Electrochemical Reactions within Au-YSZ Thin Films *via* Absorption Shifts in the Au Nanoparticle Surface Plasmon Resonance. *J. Phys. Chem. C* **2008**, *112*, 6749–6757.
32. Novo, C.; Funston, A. M.; Gooding, A. K.; Mulvaney, P. Electrochemical Charging of Single Gold Nanorods. *J. Am. Chem. Soc.* **2009**, *131*, 14664–14666.
33. Byers, C. P.; Hoener, B. S.; Chang, W. S.; Yorulmaz, M.; Link, S.; Landes, C. F. Single-Particle Spectroscopy Reveals Heterogeneity in Electrochemical Tuning of the Localized Surface Plasmon. *J. Phys. Chem. B* **2014**, *118*, 14047–14055.
34. Dondapati, S. K.; Ludemann, M.; Müller, R.; Schwieger, S.; Schwemer, A.; Händel, B.; Kwiatkowski, D.; Djiango, M.; Runge, E.; Klar, T. A. Voltage-Induced Adsorbate Damping of Single Gold Nanorod Plasmons in Aqueous Solution. *Nano Lett.* **2012**, *12*, 1247–1252.

35. Haruta, M. Size- and Support-Dependency in the Catalysis of Gold. *Catal. Today* **1997**, *36*, 153–166.
36. Panayotov, D. A.; Yates, J. T. Spectroscopic Detection of Hydrogen Atom Spillover from Au Nanoparticles Supported on TiO_2: Use of Conduction Band Electrons. *J. Phys. Chem. C* **2007**, *111*, 2959–2964.
37. Panayotov, D. A.; Burrows, S. P.; Yates, J. T.; Morris, J. R. Mechanistic Studies of Hydrogen Dissociation and Spillover on Au/TiO_2: IR Spectroscopy of Coadsorbed CO and H-Donated Electrons. *J. Phys. Chem. C* **2011**, *115*, 22400–22408.
38. Lenz, D. Hydrogen Spillover on Silica: Ethylene Hydrogenation and H_2-D_2 Exchange. *J. Catal.* **1987**, *104*, 288–298.
39. Garcia-Araez, N. Enthalpic and Entropic Effects on Hydrogen and OH Adsorption on Pt(111), Pt(100), and Pt(110) Electrodes As Evaluated by Gibbs Thermodynamics. *J. Phys. Chem. C* **2011**, *115*, 501–510.
40. Karna, S. P.; Pugh, R. D.; Shedd, W. M.; Babu, B. B. K. Interaction of H^+/H^0 with O Atoms in Thin SiO_2 Films: A First-Principles Quantum Mechanical Study. *J. Non-Cryst. Solids* **1999**, *254*, 66–73.
41. Rozanov, V. V.; Krylov, O. V. Hydrogen Spillover in Heterogeneous Catalysis. *Russ. Chem. Rev.* **1997**, *66*, 107–119.
42. Takagi, S.; Hoshino, J.-i.; Tomono, H.; Tsumuraya, K. Electron Transfer from Hydrogen Molecule to Au(111) During Dissociative Adsorption: A First-Principles Study. *J. Phys. Soc. Jpn.* **2008**, *77*, 054705.
43. Joy, N. A.; Settens, C. M.; Matyi, R. J.; Carpenter, M. A. Plasmonic Based Kinetic Analysis of Hydrogen Reactions within Au−YSZ Nanocomposites. *J. Phys. Chem. C* **2011**, *115*, 6283–6289.
44. Sil, D.; Gilroy, K. D.; Niaux, A.; Boulesbaa, A.; Neretina, S.; Borguet, E. Seeing is Believing: Hot Electron Based Gold Nanoplasmonic Optical Hydrogen Sensor. *ACS Nano* **2014**, *8*, 7755–7762.
45. Bus, E.; van Bokhoven, J. A. Hydrogen Chemisorption on Supported Platinum, Gold, and Platinum-Gold-Alloy Catalysts. *Phys. Chem. Chem. Phys.* **2007**, *9*, 2894–2902.
46. Barrio, L.; Liu, P.; Rodriguez, J. A.; Campos-Martin, J. M.; Fierro, J. L. A Density Functional Theory Study of the Dissociation of H_2 on Gold Clusters: Importance of Fluxionality and Ensemble Effects. *J. Chem. Phys.* **2006**, *125*, 164715.
47. Diebold, U. The Surface Science of Titanium Dioxide. *Surf. Sci. Rep.* **2003**, *48*, 53–229.
48. Setvin, M.; Aschauer, U.; Scheiber, P.; Li, Y. F.; Hou, W.; Schmid, M.; Selloni, A.; Diebold, U. Reaction of O_2 with Subsurface Oxygen Vacancies on TiO_2 Anatase (101). *Science* **2013**, *341*, 988–991.
49. Sheng Li, X.; Zhao Li, W; Xin Chen, Y.; Wang, H. L. Enhancement of Hydrogen Spillover by Surface Labile Oxygen Species on Oxidized Pt/TiO_2 Catalyst. *Catal. Lett.* **1995**, *32*, 31–42.
50. Antonello, A.; Brusatin, G.; Guglielmi, M.; Bello, V.; Mattei, G.; Zacco, G.; Martucci, A. Nanocomposites of Titania and Hybrid Matrix with High Refractive Index. *J. Nanopart. Res.* **2011**, *13*, 1697–1708.
51. Della Gaspera, E.; Guglielmi, M.; Perotto, G.; Agnoli, S.; Granozzi, G.; Post, M. L.; Martucci, A. CO Optical Sensing Properties of Nanocrystalline ZnO−Au Films: Effect of Doping with Transition Metal Ions. *Sens. Actuators, B* **2012**, *161*, 675–683.
52. Nikoobakht, B.; El-Sayed, M. A. Preparation and Growth Mechanism of Gold Nanorods (NRs) Using Seed-Mediated Growth Method. *Chem. Mater.* **2003**, *15*, 1957–1962.
53. Orendorff, C. J.; Murphy, C. J. Quantitation of Metal Content in the Silver-Assisted Growth of Gold Nanorods. *J. Phys. Chem. B* **2006**, *110*, 3990–3994.
54. Chen, J.; Herricks, T.; Xia, Y. Polyol Synthesis of Platinum Nanostructures: Control of Morphology through the Manipulation of Reduction Kinetics. *Angew. Chem.* **2005**, *117*, 2645–2648.
55. Herricks, T.; Chen, J.; Xia, Y. Polyol Synthesis of Platinum Nanoparticles: Control of Morphology with Sodium Nitrate. *Nano Lett.* **2004**, *4*, 2367–2371.